CrossMark

Efficient nanophotocatalyt of hydrothermally synthesized Anatase TiO$_2$ nanoparticles from its analogue metal coordinated precursor

Yasser K. Abdel-Monem[1]

Abstract In this study, the hydrothermal synthesis of TiO$_2$ nanoparticles from its coordinated metal precursor via a novel modified hydrothermal method inside stainless steel autoclave has been reported. The synthesized nanoparticles were characterized via different techniques such as: XRD, XPS, TEM and SEM. The mechanism of formation has been proposed and this method is advantageous by producing pure anatase crystalline structure at mild conditions with a relatively high surface area of 208.7 m^2 g^{-1} and 19 nm in size. Finally we assessed its photocatalytic activity toward the photocatalytic degradation of methylene blue dye. The results revealed a photo-efficiency of 96 % with a degradation rate of 0.013 min^{-1}.

1 Introduction

Semiconductor photocatalysis with a primary focus on TiO$_2$ is widely used for the treatment of air and water pollutants [1]. Photocatalysis aided by Titanium dioxide nanoparticles is used in removing the organic chemicals which occur as pollutants in wastewater effluents from industrial and domestic sources [2, 3]. There are various "sensitizers" that accelerate the process. This process is a combination of heterogeneous catalysis and solar technology [4–6]. The Photocatalytic process breaks down the compounds such as alcohols, carboxylic acids, amines, herbicides and aldehydes into carbon dioxide, water and simple mineral acids [7, 8]. The main advantage of photocatalysis is that there is no further requirement for secondary disposal methods. Other treatment methods such as adsorption by activated carbon and air stripping merely concentrate the chemicals present by transferring them to the adsorbent or air and they do not convert them to non toxic wastes [9, 10]. Also as compared to other oxidation technologies, expensive oxidation methods are not required as ambient oxygen is used [11]. TiO$_2$ is the most promising semiconductor used in photolysis since it provides a good compromise between catalytic activity and stability in aqueous media [12–14].

The anatase form possesses a band gap of 3.2 eV with an absorption edge at 386 nm and the rutile form has a lower band gap of 3.02 eV with an absorption edge at 416 nm. Both the crystal forms exhibit significant photocatalytic activity, however, the anatase form has found to exhibit higher photoactivity compared to the rutile. This makes anatase have a slightly higher redox driving force than rutile, although the range of the light absorption by the former is slightly less than that by the latter [15, 16]. Anatase also has much higher surface area than rutile, leading to enhanced adsorption capability and even generation of much more active sites (such as oxygen vacancies) [17]. Furthermore, although rutile has better charge carrier mobility due to its higher crystallinity than anatase, the latter can generate more efficient charge separation due to the existence of more oxygen vacancies. Because of these advantages of anatase, it usually shows much higher photocatalytic activity than rutile [18, 19].

The key requirement of any novel study of metal oxide nanoparticles is the synthesis method. The development of systematic, facile and reproducible methods for the synthesis of metal oxide nanoparticles is a current challenge. There are several acceptable methods for the preparation of metal oxide nanoparticles such as sol–gel method [20, 21],

✉ Yasser K. Abdel-Monem
  ykabdelmonem@gmail.com

1 Department of Chemistry, Faculty of Science, Menoufia University, Shibin al-Kawm, Egypt

microemulsion method [22, 23], precipitation method and thermal decomposition [24]. Thermal decomposition is a chemical decomposition transformation caused by heat. Thermal decomposition, as a technique broadly employed in nanotechnology, is an endothermic chemical disintegration caused by heat. Heat is required to break chemical bonds in the precursor undergoing decomposition. This is a promising and easy ''top down'' technique to prepare metal oxide nanoparticles and it is essentially based in the breakdown of the material into smaller units [25, 26].

In this work, the synthesis of nanosized anatase TiO_2 has been reported via simple and novel hydrothermal method based on its analogue coordinated precursor. TFAA was assessed as both a scavenger and a morphological control agent for obtaining pure anatase nanoparticles. The synthesized nanoparticles with very high surface area revealed a relatively high photocatalytic activity toward the photodegradation of methylene blue dye.

2 Experimental

2.1 Synthesis of TiO_2 NPs

In atypical procedure, 24 ml of Trifuloroacetic acid was added to a 30 ml of a mixture of ethanol: water with molar ratio 2:1 (v/v) while stirring at 80 °C. To this mixture, 6 ml of Titanium Tetraisopropoxide was added drop wise and the mixture was kept stirring then transferred to a Teflon-lined stainless steel autoclave for 2 h at 110 °C. The obtained gel precipitate was dried in open air oven at 50 °C.

2.2 Characterization of nanoparticles

The X-ray diffraction (XRD) measurements were conducted by using X'Pert PRO Panalyticaldiffractometer with copper target and nickel filter with CuKα radiation ($\lambda = 0.154056$ nm). Measurements were performed in the range 20°–80° (2θ).

The morphology of the particleswas obtained by Scanning electron microscopy (SEM) using JEOL JSM-7001F operating at 120 kV and by transmission electron microscopy (TEM) using a Jeol JEM 1230 operating at 120 kV. The average particle size was determined statistically by counting manually 90 particles.

X-ray photoelectron spectroscopy (XPS) surface elemental analysis was conducted using a model Thermo ESCA Lab 250xi equipped with MgKα radiation (1253 eV) and operated at 23 kV and 13 mA. The binding energy was referenced to C1 s line at 284.76 eV for calibration. N_2 adsorption–desorption isotherms were measured on test samples at liquid nitrogen temperature

(−195 °C) using a model ASAP 2010 automatic Micromeritics sorptiometer (USA), equipped with an out gassing platform.

2.3 Photocatalytic activity

Methylene blue was used as representative of organic pollutant to evaluate the photocatalysts. In a 250 ml beaker 0.01 g of the catalyst was dispersed in 100 ml of 0.01 g/l methylene blue aqueous solution. The powder was dispersed in the solution dye using ultrasonic bath for 10 min in dark afterward. After another15 min of stirring in dark, to achieve adsorption–desorption equilibrium with catalysts, the zero measurement was taken then the solution was irradiated with 254 nm UV lamb while stirring. 5 ml from the solution was taken on regular intervals to monitor absorbance change.

3 Results and discussions

Trifluoroacetic acid, TFAA, can act as a capping agent, and as an acid catalyst, it can also promote the hydrolysis and inhibit the condensation reactions [27]. Like Hydrofluroic acid, HF, TFAA has shown to be a good electron scavenger too, mainly due to the strong electron withdrawing role of the $-CF_3$ group [28]. So it seems that TFAA is a promising candidate to substitute HF in the preparation of anatase nanoparticles with enhanced photocatalytic activity. TFAA species are mainly bonded to the Ti atoms in a bidentate mode (bridging or chelating) as shown in scheme 1 to yield pure anatase TiO_2 nanoparticles.

3.1 XRD of TiO_2 nanoparticles

The XRD pattern of the as-synthesized sample was shown in Fig. 1 The peaks of the powder materials are identified to corresponding (101), (004), (200), (105), (211), (204), (116), (220), (215), and (303) crystal planes. All diffraction peaks are well defined and can be perfectly assigned to the
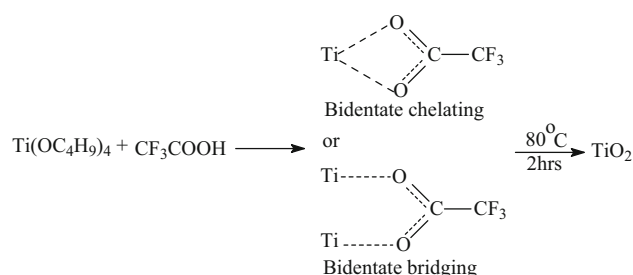
Scheme 1 Hydrothermal conversion of Ti coordinated precursor to TiO_2 NPs
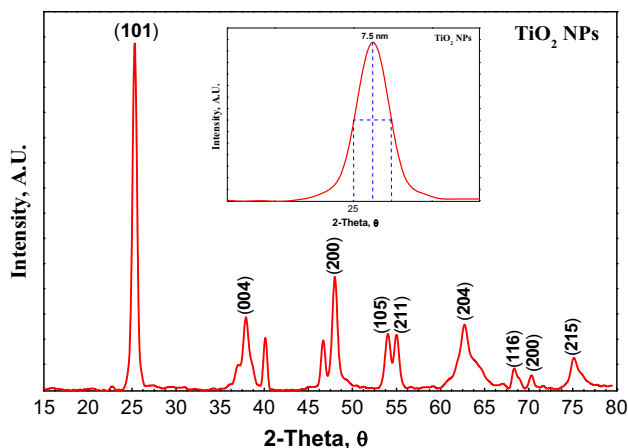
Fig. 1 XRD of pure anatase TiO_2 nanoparticles. The *inset* is the crystallite size distribution

Fig. 2 N_2 adsorption–desorption isotherms of TiO_2

anatase TiO_2 (JCPDS-21-1272). The anatase TiO_2 nanoparticles were known to be very photoactive and practical for water treatment and water purification [29]. No characteristic peaks associated with other crystalline forms were detected in the XRD pattern, indicating the anatase phase-pure nature of the product.

The crystallite size was calculated from the full width at half-maximum at the value of $2\theta = 25.4°$ using the Scherrer equation:

$$d(Å) = K\lambda/\beta \cos\theta \quad (3.1)$$

where d is the average crystallite size and the number K = 0.9 is a coefficient, $\lambda = 0.1541$ nm is the X-Ray wavelength, β is the full width half maximum (FWHM) of the catalyst, θ is the diffracting angle. The average crystallite size of as-prepared sample was calculated to be around 17 nm from the peak broadening.

3.2 N_2 adsorption–desorption isotherms of TiO_2

It is well known that the surface area, the type of adsorption isotherms, and the pore sizes/shapes are key factors in catalysis. Hence, such properties were measured using N_2sorptiometry technique. The results revealed that the Brunauer–Emmett–Teller (BET) surface area, S_{BET}, for TiO_2. The surface area, pore volumes and pore diameters of the samples are reported in Table 1. As shown in Fig. 2

Table 1 BET surface area, pore volume and size data of TiO_2

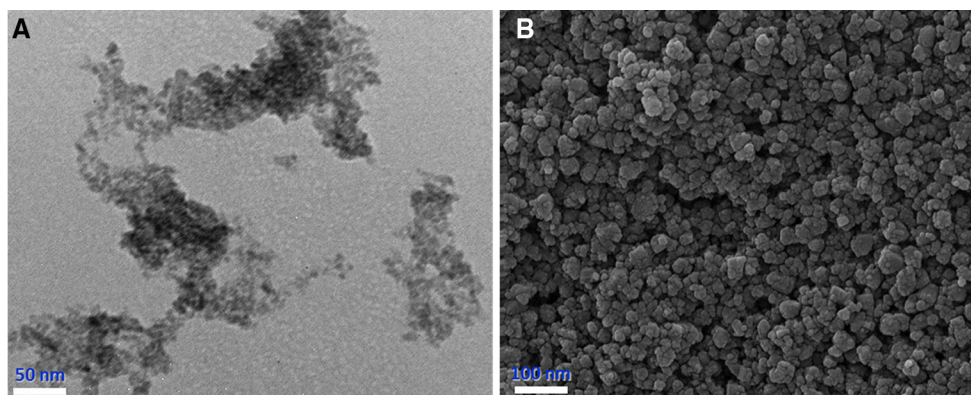|	TiO_2
BET surface area (m^2/g)	208.7
Pore volume (cm^3/g)	0.130
Pore size (nm)	7.406
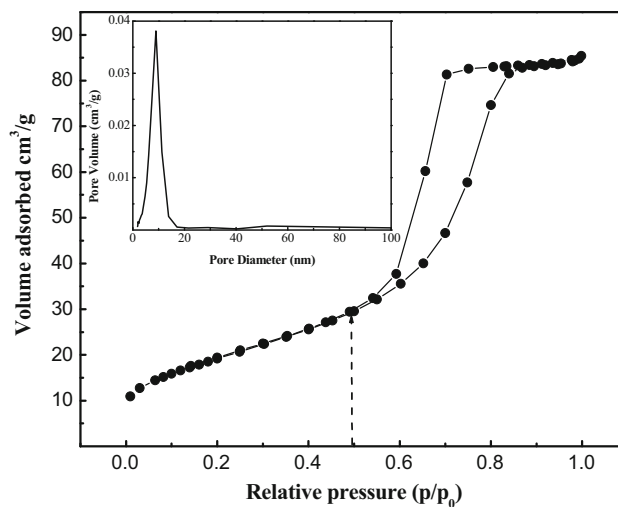
the obtained isotherms are of type-IV (indicative of mesopores in the range of 4 nm $\leq$ Dp $\leq$ 100 nm). The samples also found to exhibit type-H_2 hysteresis loops as a direct indication of cylindrical porosity of ink-bottle neck shape that is commonly found associated with compact non-uniform particles [30].

## 3.3 Electron microscopy of TiO_2

TEM analysis of TiO_2 in Fig. 3a shows that the synthesized NPs are spherical in shape. As can be seen from the TEM image that the average particle size is ~ 19 nm, which is in agreement with the crystallite, size obtained from XRD. Figure 3a reveals that the prepared titania nanoparticles are spherical and monodispersed. Also Fig. 3b presents the SEM image of TiO_2 which confirm the homogeneity in shape and particle size.

3.4 XPS of TiO_2 nanoparticles

To confirm the surface composition and oxidation state(s) of TiO_2, X-ray photoelectron spectroscopic study, XPS, was performed and the results are shown in Fig. 4 the surface oxygen (O 1 s spectrum) is attributed to O^{2-} species in TiO_2 (B.E. = 529.8 eV), a small peak appears at 531.1 eV and is assigned to OH (surface hydroxyl) [31, 32]. The binding energies of Ti $2p_{3/2}$ and Ti $2p_{1/2}$ are observed approximately at 458.8 and 464.5 eV, respectively [33]. The ratio of the areas of the two peaks A(Ti $2p_{1/2}$)/A(Ti $2p_{3/2}$) is equal to 0.5 and the binding energy difference due to the spin-orbital coupling, $\Delta E_b = E_b$(Ti $2p_{1/2}$) − E_b(Ti $2p_{3/2}$) is 5.7 eV in good agreement with the expected and reported value [34]. These two peaks are the attributes of Ti^{4+} (TiO_2).

Fig. 3 a Transmission electron microscope, **b** scanning electron microscope of TiO_2 nanoparticles after modification with stainless steel autoclave
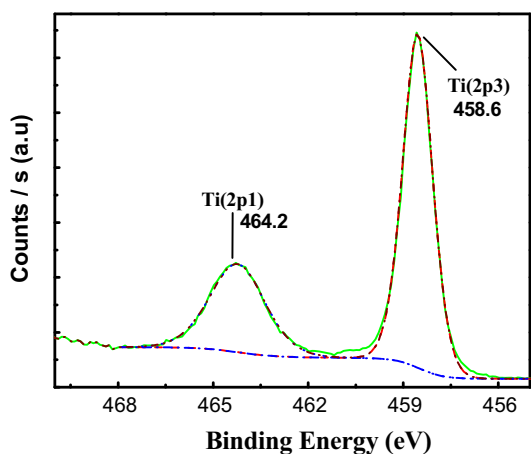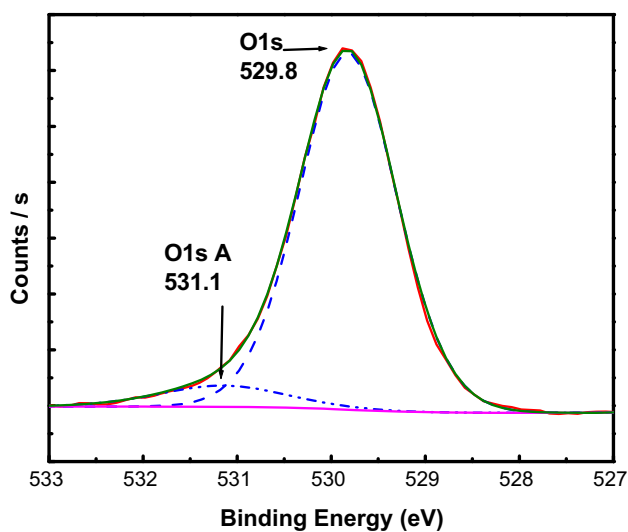

Fig. 4 Deconvoluted XPS peaks for O 1 s and Ti 2P

3.5 Photodegradation of methylene blue dye

Generally speaking, the high photocatalytic degradation rate corresponds to the high photocatalytic activity [35].

The photocatalytic ability of TiO_2 nanoparticles was evaluated by UV-degradation MB dye. Figure 5 illustrates the degradation rate of MB dye in the presence of TiO_2. The results exhibit that the obtained TiO_2 reveals superior higher photocatalytic activities up to 96 %. The photocatalytic activity of semiconductor nanoparticles depends mainly on its surface area, particle size, and band gap energy. TiO_2 has three well-known crystallographic phases in nature: anatase, rutile, and brookite [36]. It is well known that the anatase phase exhibits the maximum photoactivity. The pure anatase phase obtained in our as-prepared TiO_2 and its relatively high surface area of 209 m^2/g endow the TiO_2 nanoparticles a relative higher photocatalytic activity [37].
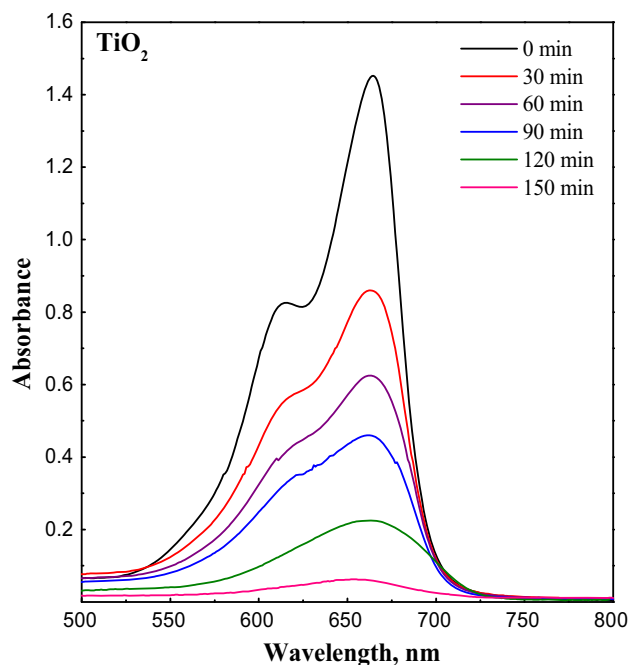
Fig. 5 UV–Vis absorption spectra revealed the photocatalytic degradation of MB dye using TiO_2 under UV irradiation

The bleaching reaction follows a pseudo-first-order reaction kinetics for the photocatalytic process, the degradation rate constant was determined from (Eq. 3.2):

$$Ln(C_0/C) = -kt \qquad (3.2)$$

where C_0 is the initial concentration and C is the concentration at time t. k is the apparent first-order rate constant. A plot of Ln C_0/C versus time represents a straight line, the slope of which upon linear regression equals the apparent first-order rate constant k (Fig. 6). The correlation constant for the fitted line was calculated to be $R = 0.994$ for TiO$_2$. The rate constants were calculated to be 0.013 min^{-1} for TiO$_2$.
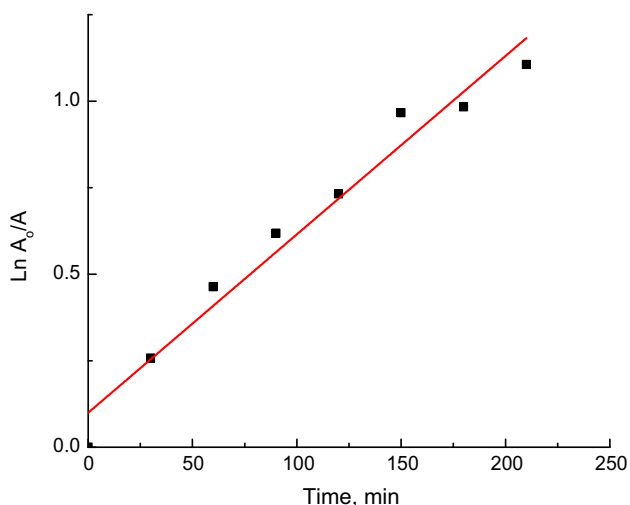
The degradation efficiency (E %) has been calculated using:

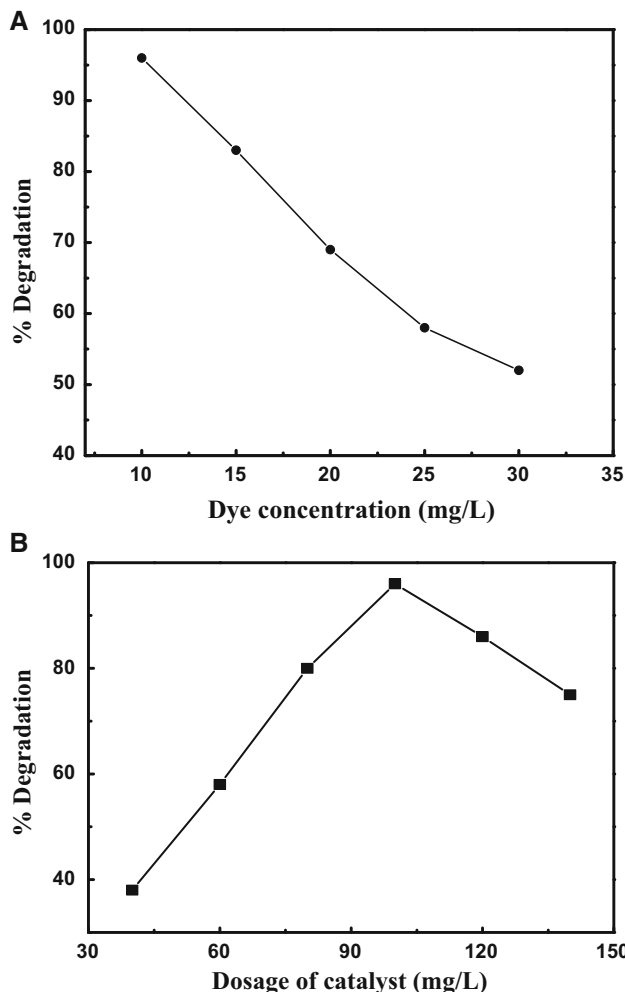$$E\% = 100 \times \left[\frac{C_0 - C}{C_0}\right] \qquad (3.3)$$

where C_0 is the initial concentration of the dye and C is the concentration of the dye after irradiation in selected time interval. The observed maximum degradation efficiency of MB is about 95.8 %.

3.6 Effect of dye concentration and catalyst dose on the photocatalytic degradation

Figure 7a shows the degradation efficiency (% D) of dye decreases with an increase in the concentration of dye. The degradation rate is directly proportional to the probability of formation of hydroxyl radicals (OH·) on the catalyst surface and the probability of hydroxyl radicals reacting with the dye molecules [38]. As the initial concentration of the dye increases, the interaction of OH radical with dye decreases. Further, increase in concentration also reduces

Fig. 7 a Effect of dye concentration on the photodegradation efficiency (% D) of MB dye and **b** photodegradation efficiency of MB dye as a function of the amount of the photocatalyst

the light penetration and the relative formation of hydroxyl radicals and super oxide radical anions decreases leading to the decreased photo degradation efficiency [39].

It is also possible that with an increase in the concentration of the dye, the amount of light that is available to excite the catalyst may decrease due to an increase in the light absorption by the dye molecules; in addition to this, for a fixed catalyst amount, the saturation of the adsorption of the dye on the surface of the catalytic particles can also be expected [39].

Figure 7b shows the photodegradation efficiency of MB (% D) as a function of the amount of the catalyst varying from 3 to 15 mg l^{-1}. Results show that % D value increases with an increase in the catalyst amount up to the optimum concentration (100 mg l^{-1}) and a further increase in the amount of the catalyst then decrease % D value, Fig. 7b. The observed enhancement in this range is probably due to an increased number of available adsorption and catalytic sites

Fig. 6 Pseudo-first-order plot for the kinetics of photodegradation of MB in TiO$_2$ under UV irradiation

on TiO_2. When the dosage of TiO_2 was increased above the limiting value, the decolourization rate decreased due to an increase in the turbidity of the suspension and a decrease in UV light penetration [40]. Therefore, the penetration depth of the photons is decreased and less catalysts nanoparticles could be activated.

4 Conclusion

Successful preparation of pure anatase TiO_2 via hydrothermal method has been reported. The characterization of the synthesized nanoparticles revealed small particle size of 19 nm with a semispherical shape and high surface area. The hydrothermally modified TiO_2 nanoparticles with its anatase from exhibited superior photocatalytic activity toward the photocatalytic degradation of MB dye. The superior photoactivity was referred to its better charge separation and high surface area.

References

1. D. Beydoun, R. Amal, G. Low, S. Mcevoy, J. Nanopart. Res. **1**, 439 (1999)
2. N. Murakami, Y. Fujisawa, T. Tsubota, T. Ohno, Appl. Catal. B: Environ. **92**, 56 (2009)
3. F. Meng, F. Lu, Z. Sun, J. Lü, Sci. China, Technol. Sci. **53**, 3027 (2010)
4. M. Ni, M.K.H. Leung, D.Y.C. Leung, K. Sumathy, Renew. Sustain. Energy Rev. **11**, 401 (2007)
5. M. Behpour, S.M. Ghoreishi, F.S. Razavi, Dig. J. Nanomater. Biostruct. **5**, 467 (2010)
6. P.C. Lansåker, J. Backholm, G.A. Niklasson, C.G. Granqvist, Thin Solid Films **518**, 1225 (2009)
7. A. Fujishima, T.N. Rao, D.A. Tryk, J. Photochem. Photobiol. C Photochem. Rev. **1**, 1 (2000)
8. S. Ahmed, M.G. Rasul, R. Brown, M.A. Hashib, J. Environ. Manage. **92**, 311 (2011)
9. V. Fierro, V.T. Torne Fernandez, D. Montane, A. Celzard, Micropor. Mesopor. Mater **111**, 276 (2008)
10. F. Woodard, *Industrial Waste Treatment Handbook* (Butterworth-Heinemann, Boston, 2001)
11. N. Nakada, H. Shinohara, A. Murata, K. Kiri, S. Managaki, N. Sato, H. Takada, Water Res. **41**, 4373 (2007)
12. G. Tian, H. Fu, L. Jing, C. Tian, J. Hazard. Mater. **161**, 1122 (2009)
13. J. Yu, J. Zhang, Dalton Trans. **39**, 5860 (2010)
14. M. Mahlambi, C. Ngila, B. Mamba, J. Nanomater. **2**, 1 (2015)
15. H.C. Liang, X.Z. Li, J. Hazard. Mater. **162**, 1415 (2009)
16. G. Li, L. Chen, M.E. Graham, K.A. Gray, J. Mol. Catal. **A275**, 30 (2007)
17. F. Li, Y. Jiang, M. Xia, M. Sun, B. Xue, D. Liu, X. Zhang, J. Phys. Chem. C **113**, 18134 (2009)
18. D.O. Scanlon, C.W. Dunnill, J. Buckeridge, S.A. Shevlin, A.J. Logsdail, S.M. Woodley, C.R.A. Catlow, M.J. Powell, R.G. Palgrave, I.P. Parkin, G.W. Watson, T.W. Keal, P. Sherwood, A. Walsh, A.A. Sokol, Nat. Mater. **12**, 798 (2013)
19. Z. Luo, A.S. Poyraz, C.-H. Kuo, R. Miao, Y. Meng, S.-Y. Chen, T. Jiang, C. Wenos, S.L. Suib, Chem. Mater. **27**, 6 (2014)
20. R. Kaur, A. V. Singh, and R. M. Mehra, J. Non-Cryst. Solids **352**(23–25), 2335 (2006)
21. J. Zhang, H. Feng, W. Hao, and T. Wang, J. Sol–Gel Sci. Technol. **39**(1), 37 (2006)
22. W. Dong, C. Zhu, Opt. Mater. **22**, 227 (2003)
23. D. Sarkar, D. Tikku, V. Thapar, R. S. Srinivasa, K. C. Khilar, Colloids Surf. A **381**(1–3), 123 (2011)
24. M. Ristic, S. Popovic, S. Music, Mater. Lett. **58**, 2494 (2004)
25. R. F. K. Gunnewiek, C. F. Mendes, R. H. G. A. Kiminami, Mater. Lett. **129**, 54 (2014)
26. M. I. Khalil, M. M. Al-Qunaibit, A. M. Al-zahem, J. P. Labis, Arabian J. Chem. **7**, 1178 (2014)
27. X. Meng, L. Qi, Z. Xiao, S. Gong, Q. Wei, Y. Liu, M. Yang, F. Wang, J. Nanopart. Res. **14**, 1 (2012)
28. S.C. Padmanabhan, S.C. Pillai, J. Colreavy, S. Balakrishnan, D.E. McCormack, T.S. Perova, Y. Gunko, S.J. Hinder, J.M. Kelly, Chem. Mater. **19**, 4474 (2007)
29. K. Lv, B. Cheng, J. Yu, G. Liu, P.C.C.P. Phys, Chem. Chem. Phys. **14**, 5349 (2012)
30. X. Wei, G. Zhu, J. Fang, J. Chen, Int. J. Photoenergy **2013**, 6 (2013)
31. S.J. Gregg, K.S.W. Sing, *Adsorption, Surface Area, and Porosity* (Academic Press, New York, 1982)
32. X. Deng, A. Verdaguer, T. Herranz, C. Weis, H. Bluhm, M. Salmeron, Langmuir **24**, 9474 (2008)
33. S. Zhu, S. Liang, Q. Gu, L. Xie, J. Wang, Z. Ding, Appl Catal B **119–120**, 146 (2012)
34. J.-G. Kang, Y. Sohn, J. Mater. Sci. **47**, 824 (2012)
35. C.D. Wagner, W.M. Riggs, L.E. Davis, J.F. Moulder, G.E. Mullenberg, in *Handbook of X-ray Photoelectron Spectroscopy*, ed. by G.E. Muilenberg (Perkin-Elmer, Eden Prairie, MN, 1979)
36. B. Ohtani, O.O. Prieto-Mahaney, D. Li, R. Abe, J. Photochem. Photobiol. A **216**, 179 (2010)
37. T.Y. Han, C.F. Wu, C.T. Hsieh, J. Vac. Sci. Technol. B **25**, 430 (2007)
38. W.Z. Tang, H. An, Chemosphere **31**, 4157 (1995)
39. P. Kuma, R. Sivakumar, S. Anandan, J. Madhavan, P. Maruthamuthu, M. Ashokkumar, Water Res. **42**, 4878 (2008)
40. M.A. Behnajady, N. Modirsahla, M. Shokri, B. Rad, Global NEST J. **10**, 1 (2008)